Polymer stabilized SnO_2 quantum-dot electron transporters for efficient perovskite solar cells

Minjin Kim[1#], Jaeki Jeong[2#], Haizhou Lu[2#], Tae Kyung Lee[3], Felix T. Eickemeyer[2], Yuhang Liu[2], In-woo Choi[1], Seung Ju Choi[1], Yimhyun Jo[1], Hak-Beom Kim[1], Sung-In Mo[1], Young-Ki Kim[4], Heunjeong Lee[5], Na Gyeong An[6], Shinuk Cho[5], Wolfgang R. Tress[7], Shaik M. Zakeeruddin[2], Anders Hagfeldt[8], Jin Young Kim[6], Michael Grätzel[2*], Dong Suk Kim[1*]

[1]Ulsan Advanced Energy Technology R&D Center, Korea Institute of Energy Research, 25 Techno saneop-ro 55beon-gil, Nam-gu, Ulsan 44776, Republic of Korea.
[2]Laboratory of Photonics and Interfaces, Institute of Chemical Sciences and Engineering, École Polytechnique Fédérale de Lausanne (EPFL), CH-1015 Lausanne, Switzerland.
[3]Photovoltaics Research Department, Korea Institute of Energy Research (KIER), 152 Gajeong-ro, Yuseong-gu, Daejeon 34129, Republic of Korea.
[4]Central Research Facilities (UCRF), Ulsan National Institute of Science and Technology (UNIST), UNIST-Gil 50, Ulsan, 44919, Republic of Korea.
[5]Department of Physics and Energy Harvest Storage Research Center, University of Ulsan, Ulsan 44610, Republic of Korea.
[6]Department of Energy Engineering, School of Energy and Chemical Engineering, Ulsan National Institute of Science and Technology (UNIST), UNIST-Gil 50, Ulsan, 44919, Republic of Korea.
[7]Novel Semiconductor Devices Group, Institute of Computational Physics, Zurich University of Applied Sciences, Wildbachstr. 21, 8401 Winterthur, Switzerland.
[8]Department of Chemistry, Ångström Laboratory, Uppsala University, Box 523, 751 20 Uppsala, Sweden.

[#]These authors contributed equally to this work.
*Correspondence to: michael.graetzel@epfl.ch (M.G.), kimds@kier.re.kr (D.S.K).

Abstract

Improvements to perovskite solar cells (PSCs) have focused on improving their power conversion efficiency (PCE) and operational stability and maintaining high performance upon scale up to module sizes. We report that by replacing the commonly used mesoporous-TiO_2 electron transport layer (ETL) with a thin layer of polyacrylic-acid-stabilized SnO_2 quantum dots (paa-QD-SnO_2) enhanced light capture and largely suppressed non-radiative recombination at the ETL-perovskite interface. The use of paa-QD-SnO_2 as electron selective contact enabled PSCs (0.08 square centimeters) with a PCE of 25.7% (certified 25.4%) and high operational stability and facilitated the scale up of the PSCs to larger areas. PCEs of 23.3, 21.7, and 20.6% were achieved for PSCs with active areas of 1, 20, and 64 square centimeters, respectively.

Main text

Efforts to realize metal halide perovskite solar cells (PSCs) with power-conversion efficiencies (PCEs) >23% have focused on formamidinium-rich lead iodide ($FAPbI_3$) formulations (*1-7*) because their narrower bandgap is closer to the Shockey-Queisser optimum than for methylammonium-based or mixed-halide perovskites (*8*). By fully using the broad absorption spectrum of $FAPbI_3$, a certified PCE of 25.21% with a short-circuit current density (J_{sc}) of >26

mA/cm^2 was obtained for the mesoporous-structure PSCs (*7*). However, the mesoporous-TiO_2 (m-TiO_2) electron-transport layer (ETL) may show unwanted photocatalytic effects under ultraviolet (UV) light illumination and the low electron mobility of m-TiO_2 limits the charge transport (*9-11*).

Among alternative metal oxide ETLs (*10-17*) for PSCs, SnO_2-based PSCs could potentially be more efficient and stable given that SnO_2 is UV resistant, has a higher carrier mobility than TiO_2 that facilitates electron extraction and transport (*10-12*). Several techniques, such as spin coating (*11, 16*), atomic layer deposition (*1*) and chemical bath deposition (CBD) (*12, 17*), have been used to deposit the SnO_2 ETLs. Spin-coated SnO_2 ETL from a SnO_2 colloidal quantum dots (QD-SnO_2) solution onto the indium doped tin oxide (ITO) substrate enabled a certified PCE of >23% for the corresponding planar-structure PSCs (*2, 16*). Recently, a thin SnO_2 ETL on fluorine-doped tin oxide (FTO) deposited with a well-controlled CBD method enabled PSCs with a certified PCE of 25.19% because of the improved carrier properties of SnO_2 ETL (*17*). However, compared with the m-TiO_2-based PSCs, the SnO_2-based PSCs still suffered from a relatively low J_{sc} of <26 mA/cm^2, that is attributed to the optical losses arising from reflection and destructive interference of the incident light waves at the interfaces.

One approach to reduce these optical losses is to use the textured surface of FTO as the front contact which scatters the incoming radiation, destroying the coherence of the incoming light and affording light trapping by increasing the optical path length (*18*). The enhanced light absorption by the perovskite benefits the photocurrent delivered by the photovoltaic (PV) cell. Similar strategies have been used for textured crystalline-silicon based PSCs (*19*). However, early efforts to deposit a thin, uniform and high-quality SnO_2 ETL using a solution process were incompatible with the underlying textured FTO surface (*1, 12, 20-22*), causing optical losses. The highest reported J_{sc} of SnO_2-based PSCs of ~25.2 mA/cm^2 (*17, 20*) still limits the overall PV performance.

Here we introduce a new architecture for the ETL of PSCs that consists of a compact-TiO_2 (c-TiO_2) blocking layer covered by a thin layer of polyacrylic-acid (PAA)-stabilized-QD-SnO_2 (paa-QD-SnO_2) deposited in a contiguous and conformal manner on the textured FTO. The uniform bilayer of paa-QD-SnO_2@c-TiO_2 largely improved the perovskite's absorption of sun light and formed an outstanding electron-selective contact with the perovskite film. The quantum size effect increased the band gap of the QD-SnO_2 from 3.6 eV for bulk SnO_2 to ~4 eV (*21, 23*) and produced a corresponding upward shift of its conduction band edge energy. This shift aligned it well with the conduction band edge of the perovskite so that electron capture by the SnO_2-based ETL proceeded with minimal energy losses (*5, 11, 16, 21*).

PAA, a polymer binder, was added to the SnO_2 QDs solution to attach the colloidal QD-SnO_2 firmly to the c-TiO_2 surface providing a contiguous, thin, and conformal SnO_2 layer that fully covered the c-TiO_2 layer underneath. Importantly, the carboxyl groups of PAA undergo strong hydrogen and coordinative bonding with the metal oxide surface, facilitating the lamination process, especially for production on a large scale (*24-26*). By choosing FTO substrates with suitable diffuse transmittance and reflectance, the textured paa-QD-SnO_2@c-TiO_2 bilayer enabled a PCE of 25.7% (certified 25.4%) with a J_{sc} of 26.4 mA/cm^2 and high stability for the corresponding PSCs. We further demonstrate that the paa-QD-SnO_2@c-TiO_2 bilayer could be applied to realize large PSC modules with an active area up to 64 cm^2 maintaining a PCE of >20%.

We investigated the microstructures of the spin-coated QD-SnO_2 layer on the c-TiO_2 using commercially available SnO_2 colloidal QDs with and without PAA. Unless otherwise mentioned, the QD-SnO_2 solution was diluted by deionized water (1:20) in this study. Fig. S1, a-c, show the top-view scanning electron microscope (SEM) images of the c-TiO_2, QD-SnO_2@c-TiO_2 and paa-QD-SnO_2@c-TiO_2, respectively. Because of the textured surface, the c-TiO_2 layer was not fully covered by the spin-coated QD-SnO_2 (Fig. S1b). In contrast, a uniform, conformal paa-QD-SnO_2 layer was formed (Fig. S1c). Atomic force microscopy (AFM) images (Fig. S1, d-f) further confirmed the uniform morphology of the paa-QD-SnO_2@c-TiO_2 (Fig. S1f), which is different from that of the QD-SnO_2@c-TiO_2 (Fig. S1e).

Fig. 1, A and B, show the cross-sectional transmission electron microscopy (TEM) images of the QD-SnO_2@c-TiO_2 and paa-QD-SnO_2@c-TiO_2 bilayers on FTO substrates, respectively. The QD-SnO_2@c-TiO_2 bilayer presented an ununiform distribution over the FTO surface with a thickness varied from ~30 (vertex region) to ~70 nm (valley region), while the paa-QD-SnO_2@c-TiO_2 bilayer had a uniform and conformal distribution over the FTO surface with a uniform thickness of ~30 nm. The different distribution between QD-SnO_2 and paa-QD-SnO_2 layers can also be seen clearly from the cross-sectional SEM images (Fig. S2, a and b), suggesting that PAA played a key role in forming the uniform and contiguous layer of paa-QD-SnO_2 ETL as shown in Fig. S3.

Element mapping with energy-disperse x-ray spectroscopy (EDS) of Ti (Fig. 1, C and D) and Sn (Fig. 1, E and F) revealed a coverage of TiO_2 and SnO_2 over the FTO surface for both QD-SnO_2@c-TiO_2 and paa-QD-SnO_2@c-TiO_2 bilayers. The selected area electron diffraction (SAD) generated by TEM for the paa-QD-SnO_2@c-TiO_2 bilayer (Fig. S4) showed that both QD-SnO_2 and c-TiO_2 were polycrystalline. The paa-QD-SnO_2 had a particle size of ~4 nm (Fig. S4c), which is also confirmed by the TEM images (Fig. S5, a-c) and dynamic light scattering analysis (Fig. S5, d and e).

The interactions between PAA and QD-SnO_2 were studied by the x-ray photoelectron spectroscopy (XPS) (Fig. S6) and fourier transform infrared spectroscopy (FTIR) measurements (Fig. S7). It is clear from the XPS measurements that both QD-SnO_2@c-TiO_2 and paa-QD-SnO_2@c-TiO_2 bilayers showed characteristic peaks attributed to Sn (Fig. S6a); however, the Sn 3*d* peaks of paa-QD-SnO_2 shifted to high binding energy by ~0.2 eV compared with that of QD-SnO_2, indicating that PAA was bonded to the QD-SnO_2. No obvious difference was observed for the O 1*s* characteristic peaks (Fig. S6, b-d). FTIR measurements showed peaks at ~2954 and ~1716 cm^{-1} that arise from C–H and C=O stretching vibrations of PAA (Fig. S7a) and a characteristic peak at ~574 cm^{-1} of the Sn-O vibration (Fig. S7b). The Sn-O peak shifted to ~594 cm^{-1} for the paa-QD-SnO_2, and the C–H and C=O stretching vibrations shifted to ~3012 and ~1628 cm^{-1}, respectively (Fig. S7c), demonstrating that PAA interacted with QD-SnO_2 (*27*).

We chose $FAPbI_3$ as the perovskite layer and details of its fabrication can be found in the supplementary materials (SM) or the previous report (*3*). Top-view SEM images of the $FAPbI_3$ films spin-coated on different ETLs, including c-TiO_2, m-TiO_2@c-TiO_2, QD-SnO_2@c-TiO_2 and paa-QD-SnO_2@c-TiO_2 are shown in Fig. S8, a to d, respectively. Compact and dense surface morphologies were observed for all the perovskite films. Figure S9a showed identical x-ray diffraction (XRD) peak positions for all samples at 14.1° and 28.2°, which correspond to the (001) and (002) crystal planes of α-$FAPbI_3$ (*3*-*5*). All the perovskite films had identical full-width at half-maximum (FWHM) for the main (001) peak (Fig. S9b). We conclude that the

morphology and crystallinity of the perovskite films are not affected significantly by the different ETLs.

The PSCs with an active area of 0.08 cm^2 were fabricated in a conventional n-i-p structure (FTO/ETL/perovskite/OAI/spiro-MeOTAD/Au), where OAI is octylammonium iodide, spiro-MeOTAD is 2,2',7,7'-tetrakis[*N*,*N*-di(4-methoxyphenyl)amino]-9,9'-spirobifluorene. We performed the quasi-steady-state current-voltage (QSS-*IV*) measurement (Fig. 2A), which was employed for the certification of PSCs by the National Renewable Energy Laboratory (NREL) and Newport Inc. Details of the QSS-*IV* measurements are given in the SM. All the PSCs were fully aged in the ambient condition for 100 hours before the measurements.

The c-TiO_2-based cell had a low PCE of 17.27% under the QSS-*IV* measurement. For the m-TiO_2@c-TiO_2 based PSC, a PCE of 23.74% with a short-circuit current density (J_{sc}) of 25.74 mA/cm^2, an open-circuit voltage (V_{oc}) of 1.142 V and a fill-factor (FF) of 80.79% was obtained, which is consistent with the previous reports (*3, 7*). Compared with the mesoporous-structured devices, the QD-SnO_2@c-TiO_2 based cell had a higher V_{oc} of 1.164 V, but a lower J_{sc} of 25.12 mA/cm^2, resulting a PCE of 23.29%. The J_{sc} of the QD-SnO_2@c-TiO_2-based PSC is similar to the values reported for the SnO_2-based cells in the literature (*17, 20*). With the paa-QD-SnO_2@c-TiO_2 ETL, the PSC exhibited a high PCE of 25.18% with a considerably improved J_{sc} of 26.28 mA/cm^2, V_{oc} of 1.177 V and FF of 81.49%, matching the 25.39% efficiency certified by Newport Inc (Figs, S10 and S11).

The conventional *J-V* measurements under both forward and reverse scans were also performed (Fig. S12). The detailed PV parameters are summarized in table S1. There is a significantly different PV value obtained for the c-TiO_2-based cell under QSS-*IV* (Fig. 2A) and conventional *J-V* measurements (Fig. S12a), while the other cells showed similar PV results, indicating that c-TiO_2-based cell is unstable and the single c-TiO_2 layer is not a proper ETL for PSCs (*28, 29*). The contrasting feature of the c-TiO_2-based cell compared to the other cells in Fig. 2A and Fig. S12a is discussed in note S1. Hereafter, the c-TiO_2-based cells will not be discussed. A statistic distribution of the PCE of all the PSCs (Fig. 2B) showed that the paa-QD-SnO_2@c-TiO_2-based PSC had the highest averaged values. Details of the statistic PV parameters of all different ETL-based cells are shown in Fig. S13. Hereafter, we chose the paa-QD-SnO_2@c-TiO_2-based cell as the target in the following discussions.

The J_{sc} of the PSCs measured under the solar simulator was verified with external quantum efficiency (EQE) measurements. The target cell had slightly higher EQE than the m-TiO_2@c-TiO_2-based PSC over the entire absorption spectrum (Fig. 2C), resulting in a higher integrated J_{sc} of 26.01 mA/cm^2; however, a relatively lower integrated J_{sc} of 25.06 mA/cm^2 was obtained for the QD-SnO_2@c-TiO_2-based device than that (25.69 mA/cm^2) of m-TiO_2@c-TiO_2-based cell. The high J_{sc} of the target cell was attributed to the desired light scattering that prolongs the optical length, enhancing the light absorption by the perovskite with the conformal structured paa-QD-SnO_2@c-TiO_2 bilayer over the FTO substrate. This is confirmed with the highest diffuse transmittance (haze) of paa-QD-SnO_2@c-TiO_2 when compared to the other ETLs shown in Fig. S14a. The higher transmittance of paa-QD-SnO_2@c-TiO_2 than the QD-SnO_2@c-TiO_2 (Fig. S14b) may be traced back to the thinner film thickness as shown in the optical simulations (Fig. S14, c and d), which could also contribute to the high J_{sc}. We further compared the J_{sc} obtained for the paa-QD-SnO_2@c-TiO_2-based PSCs using different substrates (Fig. S15). The Asahi FTO glass with high diffuse transmittance was the most suitable substrate for achieving a high J_{sc}.

The effect of the ETL composition on the photon flux emitted by the PSCs measured in steady-state at an excitation photon flux equivalent to 1 sun is shown in Fig. 2D. The investigated devices were complete solar cells without the Au back contact. Compared to the m-TiO_2@c-TiO_2 and QD-SnO_2@c-TiO_2 based devices, the target cell had significantly higher photoluminescence (PL) intensity, reaching a PL quantum yield (PLQY) of 7.5%. This indicates a reduced non-radiative recombination at the interface between perovskite and paa-QD-SnO_2 ETL. Details of the measurements and calculations of PLQY are shown in note S2. From the PLQY measurements, we derived the quasi-Fermi level splitting (ΔE_F) in the perovskite under 1 sun illumination (note S3) and compared the (ΔE_F) with the V_{oc} measured from the same device. ΔE_F and V_{oc} showed the same trend indicating that the V_{oc} increase can be partly attributed to the reduced non-radiative recombination. The $\Delta E_F/q$-V_{oc} offset (where q is the elementary charge), however, is different. For the target cell it is 10 mV lower than that of the m-TiO_2@c-TiO_2 based cells, indicating a better energetic alignment at the interfaces (*30*).

Ultraviolet photoelectron spectroscopy (UPS) measurements on the surface of different ETLs (Fig. S16) showed that the conduction band of paa-QD-SnO_2 matched better with perovskite than the m-TiO_2@c-TiO_2, which could facilitate the charge transfer from perovskite to the ETL (Fig. S17). Detailed analysis of the UPS data is shown in note S4. Fig. S18, a and b, show the time-resolved PL (TRPL) spectra of the perovskite films on different ETLs measured from both the perovskite and the glass sides. The perovskite film deposited on paa-QD-SnO_2@c-TiO_2 had the fastest decay among all the samples. Since it has low non-radiative recombination rate, the fast decay is dominated by the favored interfacial electron transfer. The electron mobility measurements (Fig. S18c) revealed that the paa-QD-SnO_2@c-TiO_2 layer had the highest carrier mobility. All these results indicate a superior charge extraction from perovskite to the paa-QD-SnO_2 ETL.

Regarding the reduced non-radiative recombination, we determined the EQE of electroluminescence (EQE_{EL}) on representative PSC devices. Fig. 2E shows an EQE_{EL} of 12.5% for the target cell at an injection current density of 26 mA/cm^2 corresponding to the J_{sc} under 1 sun illumination, whereas the m-TiO_2@c-TiO_2 and QD-SnO_2@c-TiO_2 based cells have an EQE_{EL} of 2.5% and 8.3%, respectively, under the same conditions. Thus, the non-radiative recombination rate in the PSC was reduced over 5 times simply by replacing the m-TiO_2 with a paa-QD-SnO_2 electron-selective contact layer. The obtained highest V_{oc} of 1.22 V (Fig. S19), [which is near the V_{oc} predicted from EQE_{EL} according to the reciprocity theorem (*31, 32*)] measured without the metal mask reached 98% of the radiative limit V_{oc} (1.25 V) (*2, 5*). We also conducted transient photovoltage measurements for the PSCs (Fig. S20a). The target cell showed a slower V_{oc} decay than the reference cells, indicating a slower charge recombination rate. The dark *J-V* curves (Fig. S20b) showed the lowest reverse saturation current for the target cell, pushing the on-set of the dark current to highest voltages, which also reflected the lowest interfacial non-radiative recombination.

Fig. 2F shows the light-intensity dependent V_{oc} measurements for the PSCs. For both the reference and target cells, the measured V_{oc} was linearly dependent on the logarithm of the light intensity. The diode ideality factor n_{id}, deduced from the slope described by $n_{id}k_BT/q$, where k_B is the Boltzmann constant and T is temperature, was 1.83, 1.79 and 1.46 for the the m-TiO_2@c-TiO_2, QD-SnO_2@c-TiO_2 based cells and the target cell, respectively. The reduced n_{id} contributed to the increased FF of the target cell as the FF critically depends on the n_{id} (33). The reduced n_{id} is also consistent with the PLQY, TRPL, EQE_{EL}, transient photovoltage decay and dark *J-V* measurements, unambiguously supporting the conclusion of reduced non-radiative recombination of the target PSC using paa-QD-SnO_2 ETL. This manifests itself by

much stronger photo- and electroluminescence (Fig 2, C and D) as well as a lower ideality factor (Fig. 2E) enabling very high fill factor of 83.8 % to be reached by our target device (table S2). Further strong support for our conclusion comes from the observation of a slower transient photovoltage decay (Fig. S20a) and higher electron mobility (Fig. S20b) as well as the dark *J-V* measurements of the paa-QD-SnO_2@c-TiO_2 based cell compared to the control devices. The significant reduction of the trap-assisted non-radiative recombination is the main reason for the reduced V_{oc} deficit of our target cell of ~310 mV as compared to ~350 mV for the mesoporous-structure cell [bandgap of our perovskite film was calculated to be 1.53 eV (*3*)], which is one of the lowest values reported in the field of PSCs.

Scaling up of the PSCs to module size is another requirement for their commercial exploitation. We used paa-QD-SnO_2@TiO_2 ETL to fabricate perovskite solar mini-modules with active areas up to 64 cm^2. Details of the fabrication process for the solar modules can be found in the SM and movie S1. Fig. 3A shows the *J-V* curves and images of the perovskite mini modules with different active areas. The highest PCEs achieved for the PSCs with active areas of 1, 20 and 64 cm^2 were 23.3%, 21.7% and 20.6%, respectively. Movie S2 shows a typical measurement for the 64 cm^2 perovskite solar modules. Fig. S21a illustrates a solar module with sub-cells connected in series with a magnified view of the contact connections and a geometrical FF (GFF) was calculated to be 95.6% according to the SEM images (Fig. S21b) of the interconnections. Details of the PV parameters are summarized in table S2. The decrease of the PCE with increased device size is mainly caused by a decreased FF. The V_{oc} of the module (table S2) divided by the number of stripes is 18.5 volt /16 = 1.156 V, which is equal to the V_{oc} of the 1 cm^2 cell. Hence, there is no additional V_{oc} loss in the module. Therefore, we attribute the FF decrease to the increased series resistance, including transport layer resistances, contact resistances and interconnect resistance. We sent the PSC modules to an independent laboratory (OMA company, Republic of Korea) for certification. PCEs of 21.66% (Fig. S22) and 20.55% (Fig. S23) were confirmed for the PSC mini modules with active areas of 20 and 64 cm^2, respectively, which agreed well with the measurements in our laboratory, and are compared with other reported values in Fig. S24.

We further compared the statistical distribution of the PCEs for the mesoporous-based (Fig. 3B) and target (Fig. 3C) perovskite mini modules. For the perovskite modules with the same active area (1, 20 or 64 cm^2), the target modules had higher averaged PCE and narrower PCE distributions than the mesoporous-based modules. The averaged PCE of the 64 cm^2 PSC module increased by ~30% by simply replacing the m-TiO_2 with paa-QD-SnO_2, indicating that the paa-QD-SnO_2 could be uniformly coated on the large size substrates. The statistical distribution of the PV parameters (Fig. S25) further revealed that the V_{oc} and FF of the mesoporous-based modules decreased significantly more than that of the target PSC modules. The shunt resistance of our solar modules retained a typical value of >4000 $\Omega \cdot cm^2$ (table S3), indicating that losses from leakage currents across shunts produced during scale up are negligible. We attribute the small decrease of V_{oc} and FF for the target PSC modules to the low contact resistance (Fig. S26, a and b) because of the easier laser scribing as well as low series resistance and low interfacial defects of paa-QD-SnO_2@c-TiO_2 bilayer.

Fig. 4A shows the 1000-hour shelf life tested with unsealed devices in ambient air at 25% relative humidity (RH) and 25 °C. The target PSC retained 80% of the maximum PCE (25.7%) after 1000-hour storage, whereas the m-TiO_2@c-TiO_2 and QD-SnO_2@c-TiO_2 based PSCs decreased almost 30% and 40% of the initial efficiency, respectively, indicating that the target cell is more resistant to the moisture and oxygen than the widely used mesoporous structured PSCs. We also performed the operational stability test for the unsealed devices in a N_2

environment under MPP tracking conditions using a LED lamp with a calibrated light intensity of 100 mW/cm^2. More details about the MPP tests can be found in the SM and in the previous reports (*5, 7*). Fig. 4B shows that the target cell had higher PCE than the reference cell during the 350-hour MPP tracking test. From the detailed PV parameters during the MPP tracking measurements (Fig. S27), it's clear that the higher performance of the target PSC is because of the higher and rather stable V_{oc}, which decreased less compared with the reference cells. The main degradation of the target cell is the decline of FF (Fig. S27), which is attributed to the de-doping of lithium from the hole-transport layer (HTL) (*5, 34*).

We further tested the sealed devices under ambient conditions. Fig. S28 showed that 70.5% of the initial efficiency of the target cell retained after 700-hour light-soaking test, whereas the m-TiO_2@c-TiO_2 based cell declined 45% over the same testing time. To assess the suitability of the cells for real applications, we performed MPP stability test for the encapsulated target cell under ambient conditions. Fig. S29 showed that 95% of the initial efficiency retained for the sealed target cell after 100 hours MPP tracking and 2 hours dark recovery under ambient conditions. The substantial decline of FF is still the main reason for the performance loss. Future studies of additive-free HTLs will be conducted to enhance the stability of PSCs.

References:

(1) S. Turren-Cruz, et al. Methylammonium-free, high-performance, and stable perovskite solar cells on a planar architecture. *Science* **362**, 449-453 (2018).
(2) Q. Jiang, et al. Surface passivation of perovskite film for efficient solar cells. *Nat. Photonics* **13**, 460-466 (2019).
(3) M. Kim, et al. Methylammonium chloride induces intermediate phase stabilization for efficient perovskite solar cells. *Joule* **3**, 2179-2192 (2019).
(4) H. Min, et al. Efficient, stable solar cells by using inherent bandgap of α-phase formamidinium lead iodide. *Science* **366**, 749-753 (2019).
(5) H. Lu, et al. Vapor-assisted deposition of highly efficient, stable black-phase $FAPbI_3$ perovskite solar cells. *Science* **370**, eabb8985 (2020).
(6) H. Lu, et al. Compositional and Interface Engineering of Organic-Inorganic Lead Halide Perovskite Solar Cells. *iScience*, **23**, 101359 (2020).
(7) J. Jeong, et al. Pseudo-halide anion engineering for α-$FAPbI_3$ perovskite solar cells. *Nature* **592**, 381-385 (2021).
(8) G. E. Eperon, et al. Formamidinium lead trihalide: a broadly tunable perovskite for efficient planar heterojunction solar cells. *Energy Environ. Sci.* **7**, 982-988 (2014).
(9) T. Leijtens, et al. Overcoming ultraviolet light instability of sensitized TiO_2 with meso-superstructured orgamometal tri-halide perovskite solar cells. *Nat. Commun.* **4**, 2885 (2013).
(10) Q. Jiang, et al. SnO_2: A wonderful electron transport layer for perovskite solar cells. *Small* **14**, 1801154 (2018).
(11) Q. Jiang, et al. Enhanced electron extraction using SnO_2 for high-efficiency planar-structure $HC(NH_2)PbI_3$-based perovskite solar cells. *Nature Energy* **2**, 16177 (2017).
(12) E.H. Anaraki, et al. Highly efficient and stable planar perovskite solar cells by solution-processed tin oxide. *Energy Environ. Sci*. **9**, 3128-3134 (2016).
(13) R. Chen, et al. High-efficiency, hysteresis-less, UV-stable perovskite solar cells with cascade ZnO-ZnS electron transport layer. *J. Am. Chem. Soc*. **141**, 541-547 (2019).
(14) S.S. Shin, et al. High-performance flexible perovskite solar cells exploiting Zn_2SnO_4 prepared in solution below 100 ℃. *Nat. Commun*. **6**, 7410 (2015).
(15) S.S. Shin, et al. Colloidally prepared La-doped $BaSnO_3$ electrodes for efficient, photostable perovskite solar cells. *Science* **356**, 167-171 (2017).

(16) G. Yang, et al. Stable and low-photovoltage-loss perovskite solar cells by multifunctional passivation, *Nat. Photon.* **15**, 681-689 (2021).
(17) J.J. Yoo, et al. Efficient perovskite solar cells via improved carrier management. *Nature* **590**, 587-593 (2021).
(18) S. Manzoor, et al. Improved light incoupling in planar solar cells via improved texture morphology of PDMS scattering layer. *IEEE 44th Photovoltaic Specialist Conference,* 1228-1232 (2017).
(19) Y. Hou, et al. Efficient tandem solar cells with solution-processed perovskite on textured crystalline silicon. *Science* **367**, 1135-1140 (2020).
(20) Y. Zhang, et al. Achieving reproducible and high-efficiency (>21%) perovskite solar cells with a presynthesized $FAPbI_3$ powder. *ACS Energy Lett*. **5**, 360-366 (2020).
(21) M.M. Tavakoli, et al. Mesoscopic oxide double layer as electron specific contact for highly efficient and UV stable perovskite photovoltaics. *Nano Lett*. **18**, 2428-2434 (2018).
(22) T. Bu, et al. Universal passivation strategy to slot-die printed SnO_2 for hysteresis-free efficient flexible perovskite solar module. *Nat. Commun*. **9**, 4609 (2018).
(23) A. Das, et al. The role of SnO_2 quantum dots in improved CH_4 sensing at low temperature. *J. Mater. Chem. C* **2**, 164-171 (2014).
(24) B. Hu, et al. Understanding of pre-lithiation of poly(acrylic acid) binder: Striking the balances between the cycling performance and slurry stability for silicon-graphite composite electrodes in Li-ion batteries. *J. Power Sources* **416**, 125-131 (2019).
(25) L. Wei, et al. High performance polymer binders inspired by chemical shifting of textiles for silicon anodes in lithium ion batteries. *J. Mater. Chem. A*. **5**, 22156-22162 (2017).
(26) P. Parikh, et al. Role of polyacrylic acid (PAA) binder on the solid electrode interphase in silicon anodes. *Chem. Mater*. **31**, 2535-2544 (2019).
(27) D. Yang, et al. High efficiency planar-type perovskite solar cells with negligible hysteresis using EDTA-complexed SnO_2. *Nat. Commun.* **9**, 3239 (2018).
(28) J. Ji, et al. Two-stage ultraviolet degradation of perovskite solar cells induced by the oxygen vacany-Ti^{4+} states. *iScience* **23**, 101013 (2020).
(29) M. M. Tavakoli, et al. Surface engineering of TiO_2 ETL for highly efficient and hysteresis-less planar perovskite solar cells (21.4%) with enhanced open-circuit voltage and stability. *Adv. Energy Mater*. **8**, 1800794 (2018).
(30) P. Caprioglio, et al. On the relation between the open-circuit voltage and quasi-Fermi level splitting in efficient perovskite solar cells. *Adv. Energy Mater.* **9**, 1901631 (2019).
(31) U. Rau, Reciprocity relation between photovoltaic quantum efficiency and electroluminescent emission of solar cells. *Phys. Rev. B* **76**, 085303 (2007).
(32) W. Tress, et al. Predicting the open-circuit voltage of $CH_3NH_3PbI_3$ perovskite solar cells using electroluminescence and photovoltaic quantum efficiency spectra: the role of radiative and non-radiative recombination. *Adv. Energy Mater.* **5**, 1400812 (2015).
(33) M. Green, et al. Accuracy of analytical expressions for solar cell fill factors. *Solar Cells* **7**, 337-340 (1982).
(34) Y. Wang, et al. Stabilizing heterostructures of soft perovskite semiconductors. *Science* **365**, 687-691 (2019).
(35) N.J. Jeon, et al. Compositional engineering of perovskite materials for high-performance solar cells. *Nature* **517**, 476-480 (2015).
(36) M. Kim, et al. Effects of cation size and concentration of cationic chlorides on the properties of formamidinium lead iodide based perovskite solar cells. *Sustainable Energy Fuels* **4**, 3753-3763 (2020).
(37) R. T. Ross, et al. Some thermodynamics of photochemical systems. *J. Chem. Phys.* **46**, 4590-4593 (1967).

(38) P. Wurfel, et al. The chemical potential of radiation. *J. Phys. C: Solid State Phys.* **15**, 3967-3985 (1982).
(39) T. Kirchartz, et al. Photoluminescence-based characterization of halide perovskites for photovoltaics. *Adv. Energy Mater.* **14**, 1904134 (2020).
(40) D. Prochowicz, et al. Influence of A-site cations on the open-circuit voltage of efficient perovskite solar cells: a case of rubidium and guanidinium additives. *J. Mater. Chen. A* **7**, 8218-8225 (2019).
(41) F. Zhang, et al. Ultraviolet photoemission spectroscopy and Kelvin probe measurement on metal halide perovskites: advantages and pitfalls, *Adv. Energy Mater.*, **10**, 1903252 (2020).
(42) L.A.A. Pettersson, et al. Modeling photocurrent action spectra of photovoltaic devices based on organic thin films. *J. Appl. Phys.*, **86**, 487 (1999).
(43) M. Jeong, et al. Stable perovskite solar cells with efficiency exceeding 24.8% and 0.3-V voltage loss. *Science* **369**, 1615-1620 (2020).
(44) P. Li, et al. Inkjet manipulated homogeneous large size perovskite grains for efficient and large-area perovskite solar cells. *Nano Energy* **46**, 203-211 (2018).
(45) J.G. Tait, et al. Rapid composition screening for perovskite photovoltaics via concurrently pumped ultrasonic spray coating. *J. Mater. Chem. A* **4**, 3792-3797 (2016).
(46) F.D. Giacomo, et al. Up-scalable sheet-to-sheet production of high efficiency perovskite module and solar cells on 6-in. substrate using slot die coating. *Solar Energy Mater. and Solar cells* **181**, 53-59 (2018).
(47) Y. Deng, et al. Surfactant-controlled ink drying enables high-speed deposition of perovskite films for efficient photovoltaic modules. *Nat. Energy* **3**, 560-566 (2018).
(48) G. Fu, et al. Efficient enhancement in planar $CH_3NH_3PbI_{3-x}Cl_x$ perovskte solar cells by processing with bidentate halogenated additives. *Solar Energy Mater. and Solar cells* **165**, 36-44 (2017).
(49) E. Bi, et al. Efficient perovksite solar cell modules with high stability enabled by iodide diffusion barriers. *Joule* **3**, 2748-2760 (2019).
(50) A. Priyadarshi, et al. A large area (70 cm^2) monilithic perovskite solar module with a high efficiency and stability. *Energy Environ. Sci.* **9**, 3687-3692 (2016).

Acknowledgements:

We thank B. I. Carlsen, O. Ouellette and Minyang Wei for kind discussions. **Funding:** This work was support by Development Program of the Korea Institute of Energy Research (KIER) (C1-2401 and C1-2402), Basic Science Research Program through the National Research Foundation of Korea (NRF) funded by the Ministry of Education (NRF-2020R1A6A1A03038697), and the NRF funded by the Ministry of Science, ICT, and Future Planning (2020M1A2A2080746 and 2020M1A2A208075011). M. G. thanks the financial support from the European Union's Horizon 2020 research and innovation programme under grant agreements No 881603 and 764047. **Author contributions:** M.G. and D.S.K. designed and supervised the project. A.H., J.Y.K. and S.M.Z. advised on the research. M.K., J.J. and H.L. studied and constructed the concept, and analysed the experimental data. H.L., M. K., W.R.T., and J.J. wrote the manuscript. M.G. and D.S.K revised the manuscript. T.K.L. contributed to the optical measurements. H.L., F.T.E. and W.R.T performed the PLQY and EQE_{EL} measurements and analysis. Y.L. contributed to the characterization of the chemicals. I-.C., S.J.C., N.G.A. and Y.J. characterized the perovskite film with UV-Vis absorption, XPS, and XRD. S-.I.M. analysed the FTIR. H-.B.K. performed the UPS measurements. M.K., J.J. and H.L. performed the stability test. Y-.K.K. analysed the HR-TEM. All the authors contributed to the discussions about the manuscript and the reviewers' comments. **Competing interests:** None declared. **Data and materials availability:** All (other) data needed to evaluate

the conclusions in the paper are present in the paper or the Supplementary Materials.

Supplementary Materials:

Materials and Methods
Supplementary Text
Notes S1 to S4
Figs. S1 to S29
Tables S1 and S3
SM refs (35-50)
Movies S1 and S2

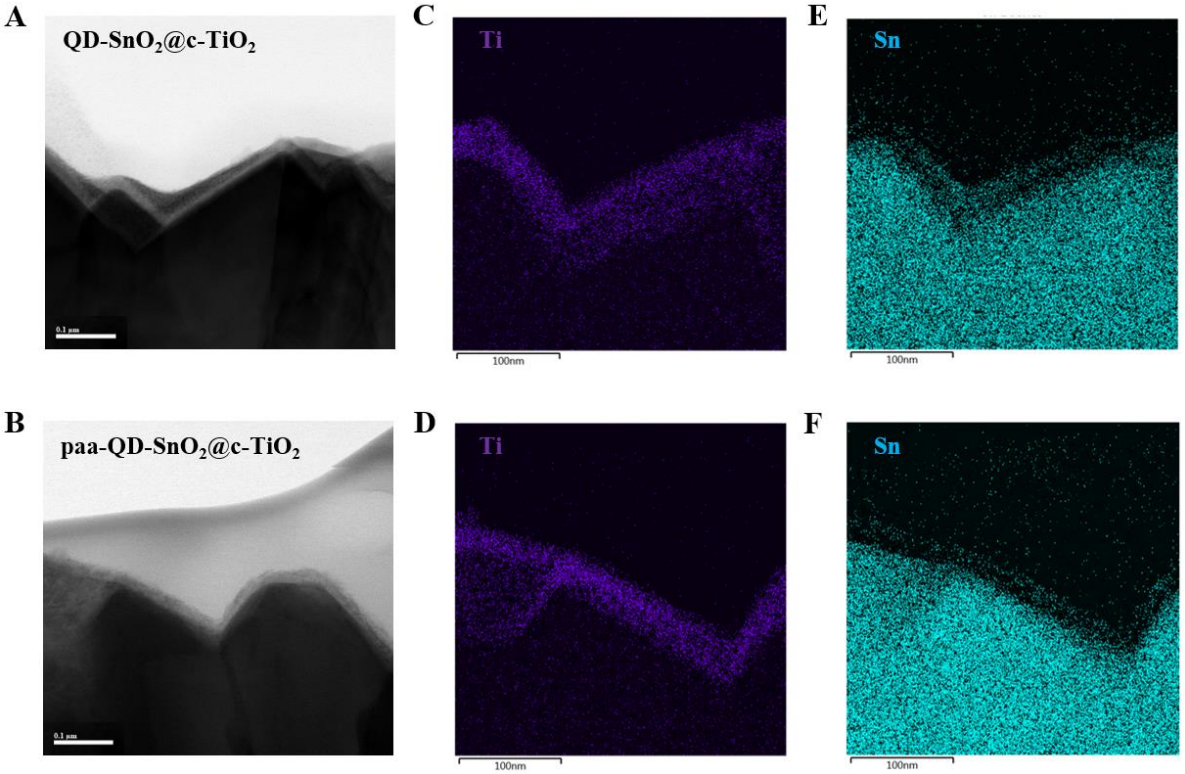

Figure 1. Microstructures of the ETLs. (**A** and **B**) The cross-sectional TEM images of the QD-SnO_2@c-TiO_2 (A) and paa-QD-SnO_2@c-TiO_2 over the FTO substrates. (**C** and **D**) EDS elemental analysis of Ti for both QD-SnO_2@c-TiO_2 (C) and paa-QD-SnO_2@c-TiO_2 (D) over the FTO surface. (**E** and **F**) EDS elemental analysis of Sn for both QD-SnO_2@c-TiO_2 (E) and paa-QD-SnO_2@c-TiO_2 (F) over the FTO surface.

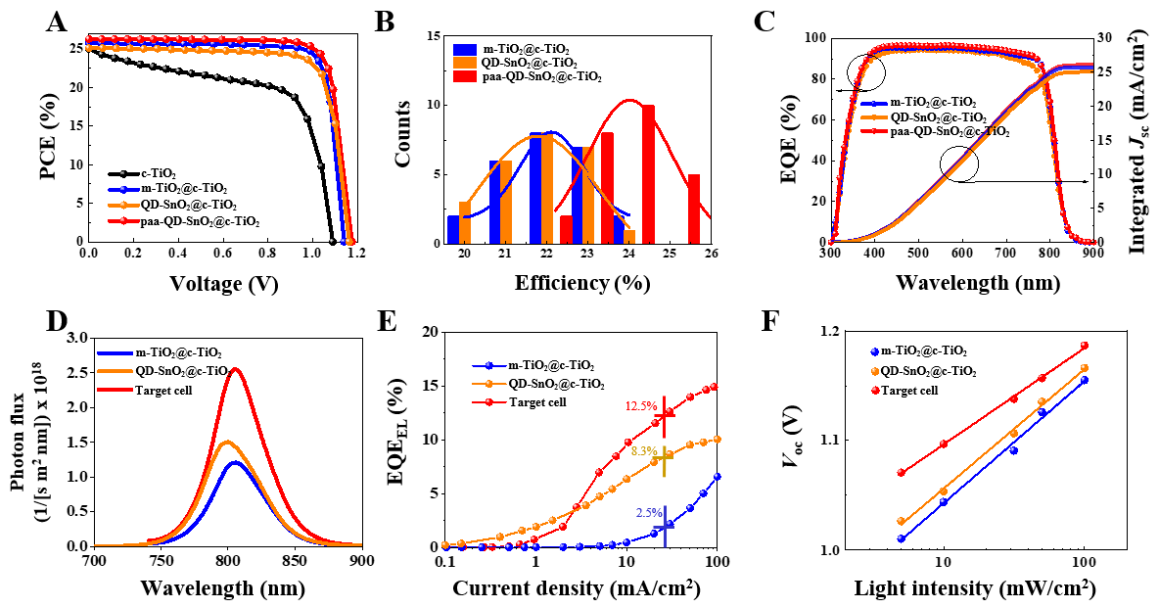

Figure 2. Characterization of the PSCs. (**A**) The *J-V* curves of the PSCs with different ETLs measured under the QSS-*IV* method. (**B**) A statistic distribution of the PCE for PSCs with different ETLs. (**C** to **F**) The EQE and integrated J_{sc} (C), Steady-state PL spectral photon flux (D), EQE_{EL} (E) and the light dependent V_{oc} (F) for the PSCs with different ETLs.

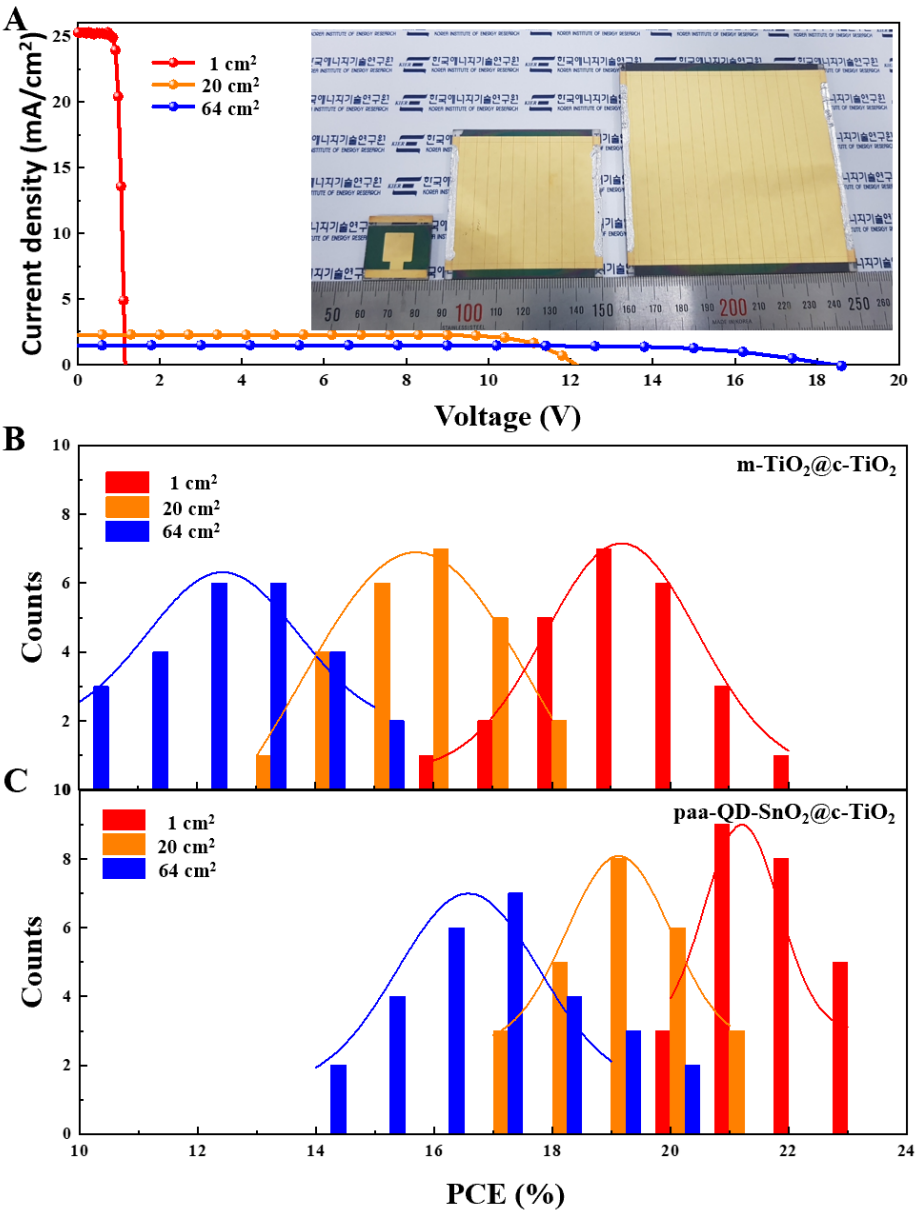

Figure 3. Performance of the large-size PSCs. (**A**) *J-V* curves of the large-size PSCs. The inserted picture is a photo images of the large-size PSCs. (**B** and **C**) Statistic distributions of the PCEs for the m-TiO_2@c-TiO_2 (B) and paa-QD-SnO_2@c-TiO_2 (C) based PSCs with pixel sizes of 1, 20 and 64 cm^2.

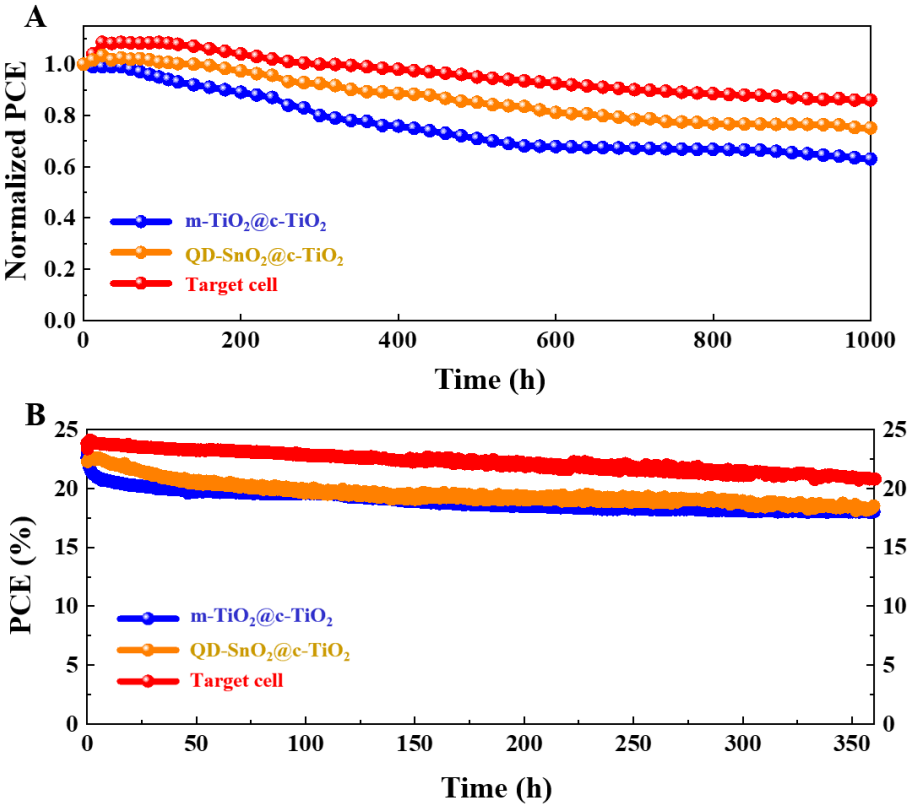

Figure 4. Stability of the PSCs with different ETLs. The stability shown here represents the best stability results of our four tested samples. (**A**) Shelf life of the unencapsulated PSCs tested in ambient air at 25% RH and 25 ℃ with different ETLs. (**B**) the operational stability test of the unencapsulated PSCs under MPP tracking conditions in a N_2 environment.